Correlative imaging reveals holistic view of soil microenvironments

Steffen Schlüter[1*] , Thilo Eickhorst[2], Carsten W. Mueller[3]

1. Department Soil System Sciences, Helmholtz-Centre for Environmental Research - UFZ, Halle, Germany

2. FB 2 (Biology/Chemistry), University of Bremen, Bremen, Germany

3. TU Munich, Chair of Soil Science, Freising-Weihenstephan, Germany

*Corresponding Author: steffen.schlueter@ufz.de

Address:

Helmholtz-Centre for Environmental Research – UFZ

Theodor-Lieser-Str. 4

06120 Halle

Germany

Abstract

The micro-environmental conditions in soil exert a major control on many ecosystem functions of soil. Their investigation in intact soil samples is impaired by methodological challenges in the joint investigation of structural heterogeneity that defines pathways for matter fluxes and biogeochemical heterogeneity that governs reaction patterns and microhabitats. Here we demonstrate how these challenges can be overcome with a novel protocol for correlative imaging based on image registration to combine three-dimensional microstructure analysis of X-ray tomography data with biogeochemical microscopic data of various modalities and scales (light microscopy, fluorescence microscopy, electron microscopy, secondary ion mass spectrometry). Correlative imaging of a microcosm study shows that the majority (75%) of bacteria are located in mesopores (<10µm). Furthermore they have a preference to forage near macropore surfaces and near fresh particulate organic matter. Ignoring the structural complexity coming from the third dimension is justified for metrics based on size and distances but leads to a substantial bias for metrics based on continuity. This versatile combination of imaging modalities with freely available software and protocols may open up completely new avenues for the investigation of many important biogeochemical and physical processes in structured soils.

1. Introduction

Small-scale heterogeneity of environmental conditions in soil exerts a major control on carbon and nutrient cycling. Physical accessibility at the pore scale plays an important role for long-term carbon stabilization[1, 2] and for microbial diversity in soil through spatial separation in diverse ecological niches[3-5]. Many microbial processes like respiration, nitrification and denitrification are known to occur in hotspots of microbial activity which are imprints of the patchy distribution of microhabitats in soil[6]. These patterns form as a result of a complex interplay between biotic and abiotic agents, so their formation cannot be understood, if individual processes are studied in isolation. This calls for a joint characterization of (i) the physical soil structure providing the pathways for matter fluxes, (ii) the chemical properties that drive local reactions in soil and (iii) the distribution of soil biota that is both resulting from and actively changing the former[7, 8].

While the three-dimensional (3D) characterization of the physical structure of intact soil has advanced tremendously with the advent of non-invasive imaging techniques like X-ray micro-tomography[9-11] (µCT), 3D imaging of biogeochemical heterogeneity in opaque soil is still not achievable. Thus, it is still common practice to cut the soil into pieces, with or without prior resin impregnation, in order to apply two-dimensional (2D) microscopic and micro-spectroscopic imaging techniques on exposed surfaces. The combination of various biogeochemical imaging methods is an emerging field in life sciences called correlative imaging or correlative microscopy[12, 13]. In contrast to the fast growing number of applications of 3D chemical imaging using fluorescence microscopy approaches, such a straightforward approach is not at hand for intact natural geological materials including opaque soil and plant-soil systems. Consequently applications in soil science are few, in particular the combination of two-dimensional biogeochemical imaging modalities with 3D non-invasive imaging. When using soil sections for

2D biogeochemical imaging, a major hurdle is to find the exact plane of the exposed surface within a bigger 3D volume. Depending on the scale gap this can turn into a search for a two-dimensional needle in the 3D haystack. One pragmatic solution is to cut or grind down the exposed surface strictly along a principle axis of the 3D image to reduce the degrees of freedom with which the 2D plane can potentially be oriented. In this way, the spatial distribution of *P. fluorescens* in fluorescence microscopy (FM) images of soil microcosms was directly related to pore space attributes measured with X-ray microtomography[14]. The more flexible approach is to pose this 2D-3D image registration as an optimization problem. In a pioneering study by ref.[15], stacks of elemental maps obtained with scanning electron microscopy coupled to energy-dispersive X-ray spectroscopy (SEM-EDX) were registered to a µCT image of resin-embedded soil. This was done by a search algorithm with three degrees of freedom (one vertical translation, two rotations) that optimized the correlation coefficient between the elemental map and the aligned µCT plane. The search was guided by reducing the 3D volume in vertical direction to the most probable region and by reducing the range of allowed rotation angles in both directions.

In this paper we present a new protocol for correlative imaging based on elastix[16, 17], a free image registration software popular in biomedical imaging. The main methodological objective is to outline best practices for successful 2D-3D image registration along the lines of ref.[15] but extended and improved in different ways. Correlative microscopy is demonstrated for various image modalities including µCT, FM, SEM-EDX, light microscopy (LM), and nano-scale secondary ion mass spectroscopy (NanoSIMS). They cover a large range of scales from a lateral resolution of 0.1 µm in nanoSIMS images to continuity of air-filled pores in a sample 2 cm in size. The LM of the entire sample cross section serves as a reference plane to which all other imaging modalities including µCT are registered. The main scientific objective of the paper is to link microhabitats with the physical structure of soil by exploring the spatial distribution of bacteria and relating it to pore architecture and substrate availability in the detritusphere around a decaying leaf. For the first time we systematically analyze the bias in habitat metrics that is introduced by ignoring structural information from the third dimension. The versatility of the image registration approach is further demonstrated by spatial alignment of SEM-EDX and NanoSIMS data.

2. Material and methods

2.1. Sample preparation

The repacked sample was composed of fine textured-soil (silt loam, derived from a subsoil horizon of a Stagnosol). Sand grains (coarse sand, 5% v/v) were amended for structural support. A poplar leaf fragment was placed in the center while the sample was repacked to a bulk density of 1.3 g cm^{-3} in a PTFE cylinder (10 mm inner diameter, 20 mm height). The soil was incubated at field capacity and room temperature for 7 days. The water used for saturation was amended with five bacterial strains (Vitabac, Bactivia GmbH, Germany) to enrich the subsoil material with soil bacteria.

After incubation the sample was chemically fixated with 2% formaldehyde solution to keep the structure of the cells and microbial nucleic acids intact. After fixation the intact cores were initially dehydrated with acetone (graded series from 70 to 100% (v/v)) and then impregnated with a series of Araldite 502:acetone mixtures (1:3, 1:1 (vl:vl)) and finally with 100% Araldite 502 (Araldite kit 502, electron microscope sciences, Hatfield, USA). The blocks were cured at 60°C for 48 h[18]. Prior to sectioning of the cylinders the samples were measured using X-ray microtomography. The cylindrical sample was cut vertically with a diamond saw (Struers Discoplan TS) to achieve a large cross-sectional area. The cut sample was subsequently polished and glued onto a round glass disc of 25.4 mm diameter. The remaining sample was cut to a thickness of approx. 0.5 mm using a diamond saw (see above, sample fixed on a vacuum holder). Finally the vertical cross section was ground down and polished to obtain a thin section with a surface of low topography[19].

2.2. Imaging

2.2.1. X-ray microtomography

After resin impregnation the intact sample was scanned with X-ray microtomography (X-tek XMT 225, Nikon Metrology, Herts UK). 2800 Projections (110 kV, 140 µA, no filter, 700ms, 2 frames per projection) were acquired and reconstructed into a 3D tomogram with a voxel length of 7µm using the X-tek Pro software. The image was filtered and segmented into pores and solid with protocols explained in ref.[20] using Fiji/ImageJ[21] and QuantIm[22]. The leaf was segmented with the region growing tool in VG Studio Max 2.1 (Volume Graphics). Occasional over-segmentation due to low contrast between leaf and resin had to be removed manually in VG Studio Max 2.1.

2.2.2. Light microscopy

The entire cross sectional area was mapped with reflected light microscopy (Zeiss AxioImager 2) using polarized light and the extended depth of focus mode. Individual images (z-stacks and mosaic images) were stitched together using the Zeiss software (Zeiss AxioVision). The 50x magnification resulted in a pixel length of 1.1 µm. Some regions of interest were scanned again at higher magnification (200 x) to map the sample surface for easier location of subsequent NanoSIMS measurements.

2.2.3. Fluorescence microscopy

A large area of the exposed surface partially covering the leaf was scanned with fluorescence microscopy (Zeiss Axiospkop 2 equipped with an HBO 103 W/2 Hg vapour lamp and Plan-Neofluar objectives 20× and 40×). The polished thin section was stained using DAPI (Vectashield H-1200), which selectively binds to DNA. Fluorescence filter sets were used to visualize DAPI-stained cells (F46-000, AHF) and organic soil compounds (double excitation, #24, Zeiss). Imaging was done with a CCD camera (Colorview II, Soft Imaging) connected to an imaging software (AnalySIS, Soft Imaging). Several images were stitched together automatically with the multiple image alignment module of the AnalySIS software and Adobe PhotoShop CS6.

2.2.4. NanoSIMS microspectroscopy

A 0.2 mm transect from the leaf into the surrounding soil was mapped using nano-scale secondary ion mass spectrometry (NanoSIMS). The NanoSIMS images were recorded with a Cameca NanoSIMS 50 L (Gennevilliers, France). Prior to the NanoSIMS measurements, an Au/Pd layer (~30 nm) was sputter coated to avoid charging during the measurements. The Cs+ primary ion beam was used with a primary ion impact energy of 16 keV. Prior to final analysis, any contaminants and the Au/Pd coating layer were sputtered away at 50 by 50 µm using a high primary beam current (pre-sputtering). During this pre-sputtering, the reactive Cs+ ions were implanted into the sample to enhance the secondary ion yields. The primary beam (ca. 1.2 pA) was focused at a lateral resolution ca. 100 nm and was scanned over the sample, with 12C-, 12C14N-, 16O-, and 56Fe16O- secondary ions collected on electron multipliers with an electronic dead time fixed at 44 ns. The estimated depth resolution with 16 keV Cs+ ions was 10 nm. The electron flood gun was used to compensate for any charging effects due to the non-conductive mineral particles (e.g. larger quartz grains). All measurements were done in imaging mode. For ion images with a field of view of 30 by 30 µm, 40 planes were acquired using a dwell time of 1 ms/pixel, with 256 pixels by 256 pixels. Images were corrected for electron multiplier dead time and the measurements stacks were accumulated using the Look@NanoSIMS software[23].

2.2.5. SEM-EDX microspectroscopy

The larger area around the NanoSIMS transect across the leaf-soil interface was scanned again with SEM-EDX (JEOL-JSM7200F). The area was scanned using the backscatter electron detector to obtain high resolution images of the detritusphere, using the material contrast to differentiate between minerals and organic tissues and resin. Additionally a mosaic at the detritus interface was analyzed using EDX at 15 keV to show the elemental distribution at a larger field of view. The resulting images were stacked using the MosaicJ plugin in Fiji/ImageJ[21].

2.3. Image Analysis

The 3D physical structure can be analyzed in various ways. In this study we are interested in microhabitats which are likely to be modulated by the presence of the leaf and by the distribution of water and air in the pore space. The water distribution during incubation is unknown, since the intact sample was only scanned after resin impregnation. However, the distribution can be modelled with a morphological approach using the maximum inscribed sphere method in combination with a connectivity rule[24]. That is, pores are assigned to air, if they can entirely fit a sphere of a certain radius and have a continuous path to the headspace of the sample from where the air invades. All smaller or disconnected pores are assigned to water. The radius is directly linked to the curvature of the air-water interface and hence related to capillary pressure through Young-Laplace's law. Thus, a step-wise decrease in radius resembles a drainage process. For any drainage step, the Euclidean distance of all non-air voxels to the closest air voxel can be computed, which gives a rough estimate of diffusion lengths of dissolved oxygen in soil that can be limiting for microbial respiration. In the same vein, Euclidean distances can be computed from

the leaf into the soil, or from the soil-pore interface into the soil or into the pore space. The pore size distribution and Euclidean distance transforms were computed with Fiji/ImageJ[21] and air continuity were evaluated with the MorpholibJ plugin[25]. The algorithm to model drainage based on pore size distribution and air continuity is explained in detail in the supporting information (S1).

The exact micro-environmental conditions during incubation cannot be recovered through image analysis. However, the spatial distribution of bacteria visualized via epifluorescence microscopy (FM images) may indicate favorable microenvironments. Even though there are dedicated protocols for automatic cell counting[26], we resorted to manual cell counting using the ROI manager in Fiji, which is still feasible for such a proof-of-concept study. The distribution of bacteria is analyzed with respect to site preference, e.g the tendency to proliferate near the leaf surface. To do so, the average Euclidean distance from a cell to the closest leaf surface is determined for a fixed number of cells (n=50) randomly chosen from the population of all manually detected cells (n=536). A normalized bacteria-leaf distance ratio is calculated by dividing the bacteria-leaf distance with the average Euclidean distance of an equal amount of randomly chosen soil voxels to the closest leaf surface. This ratio is computed repeatedly for a number of realizations (n=50) to get a robust estimate of the ratio that may either indicate preference (<1), avoidance (>1) or indifference (=1). Same is done for the distance of bacteria to pore surfaces. In addition, the relative bacteria abundance in three different pore size classes (mesopores, narrow macropores, macropores) was determined. Cells in voxel locations which were assigned to soil during µCT image segmentation are all assigned to unresolved mesopores, i.e. smaller 1-2 voxels (≈ 10µm), assuming that cells are too big to fit into unresolved micropores (<0.2µm). Cells within visible pores are further differentiated by a pore diameter threshold of 7 voxels (7 x 7µm ≈ 50µm) into narrow macropores that drain at a capillary pressure range of 60-300hPa and macropores (>50µm) that are drained at field capacity (60hPa).

2.4. Image Registration

The objective of image registration is to find a transformation matrix that aligns a moving image with a target image such that an objective function is optimized. The target image is always the light microscopy (LM) image of the entire polished surface. The moving images to be transformed are either the 3D X-ray CT image of the physical structure or various biogeochemical, spectromicroscopic images of smaller sub-sections. The objective function consists of two terms: a) the sum of Euclidean distances between corresponding landmark points set manually at easily identifiable objects in the microscopy plane and b) the mutual information criterion[27] that quantifies the entropy in a two-dimensional histogram composed of the corresponding gray values at random locations of the aligned image pairs. This mutual information criterion is more suitable to verify the alignment of images from different modalities than simple correlation coefficients since different material classes may not always have proportional intensities in both images. Image registration was carried out with the elastix software[16, 17] by employing a similarity transform with seven degrees of freedom in 3D (three

rotations, three translations and one scaling parameter) and four degrees of freedom in 2D (one rotation, two translations and one scaling parameter). Convergence was accelerated by imposing a pyramid schedule, i.e. quick registration was achieved with coarse, rescaled copies and alignments was sequentially refined at the next finer scale. Note that image registration with different dimensionality (2D vs. 3D) is not implemented in elastix so that the LM image had to be converted into a 3D image with a thickness of one slice first. A minimum example including images, landmark and parameter files and execution commands are provided as supporting information (S3).

The transformation matrix can not only be employed on the moving image for which it was optimized, but also on any other spatial data resulting from image analysis, such as point patterns of bacteria distribution in FM images or pore size maps and distance maps obtained from segmented X-ray CT images. This is done with transformix, a sub-routine of elastix, for which an example is also added as supporting information.

3. Results and Discussion

3.1. 3D Physical Structure

The 3D tomogram is cut virtually at three principle planes in Figure 1(a) to reveal to position of the embedded leaf (green). The outcome of 2D-3D image registration is a plane through the moving µCT image (Figure 1b) that is perfectly aligned with the target LM image (Figure 1c). The exact position of the LM plane is somewhat arbitrary and a result of cutting and polishing during sample preparation. However, the µCT image could in fact be used to identify points of interest and guide the positioning of microscopy planes. The eleven landmarks that helped find the plane are also depicted. The final, average distance of corresponding landmarks was 9.5µm, which corresponds to 1.4 voxels in the X-ray CT image and 8.6 pixels in the LM image. Note that even though most landmarks are deliberately set in the vicinity of the leaf, the spatial alignment of objects further away from the leaf is also excellent.

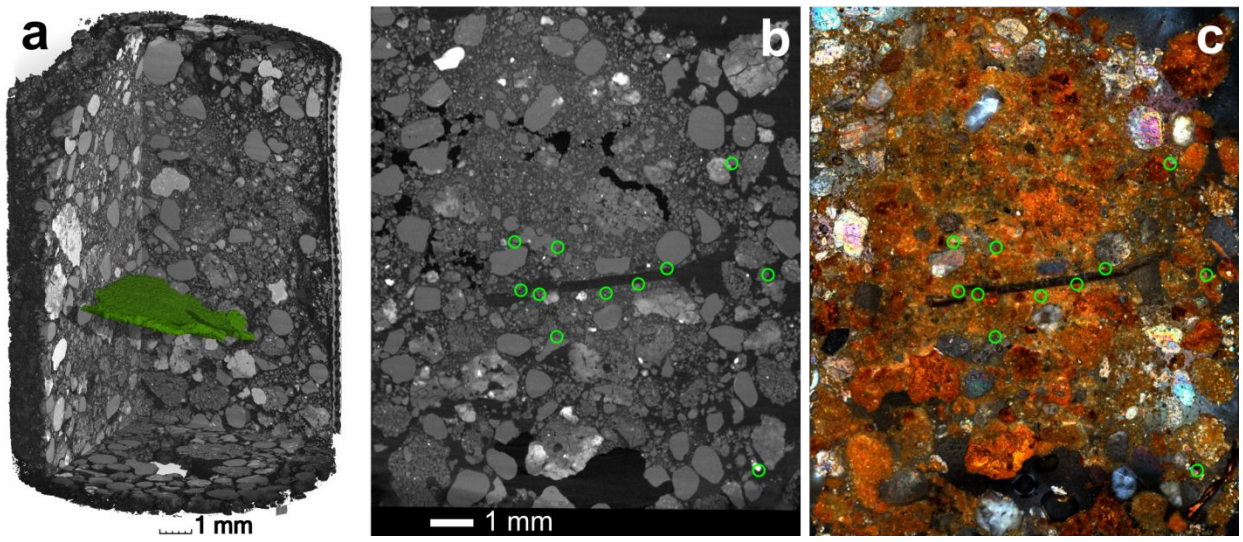

Figure 1: (a) X-ray CT scan with the embedded leaf in green. (b) 2D-3D registration and (c) the reference microscopy image that was used as a target for image registration. Eleven landmarks (green circles) were used for image registration.

After an adequate transformation matrix for the µCT gray scale data had been found, it was used to project the 3D pore size map into the LM plane (Figure 2a). Likewise, the results of a 3D drainage model based on local pore size and global air continuity were also co-registered with the LM plane (Figure 2b), just like the 3D Euclidean distance from any non-air voxel to the closest air-filled pore at a certain capillary pressure (50hPa in Figure 2c). Averaging over all soil voxels in the registered plane results in the mean air distance at this capillary pressure (Figure 2d). This decreases from 0.65mm to 0.21mm when the sample is drained from 20hPa to roughly field capacity (59hPa). The mean air distance in the leaf is a bit higher (0.82mm) at 20hPa because it is occluded in the wet soil matrix. The distance drops to 0.13mm in a narrow range around 45hPa because the small gap that formed above the leaf is invaded by air at that capillary pressure.

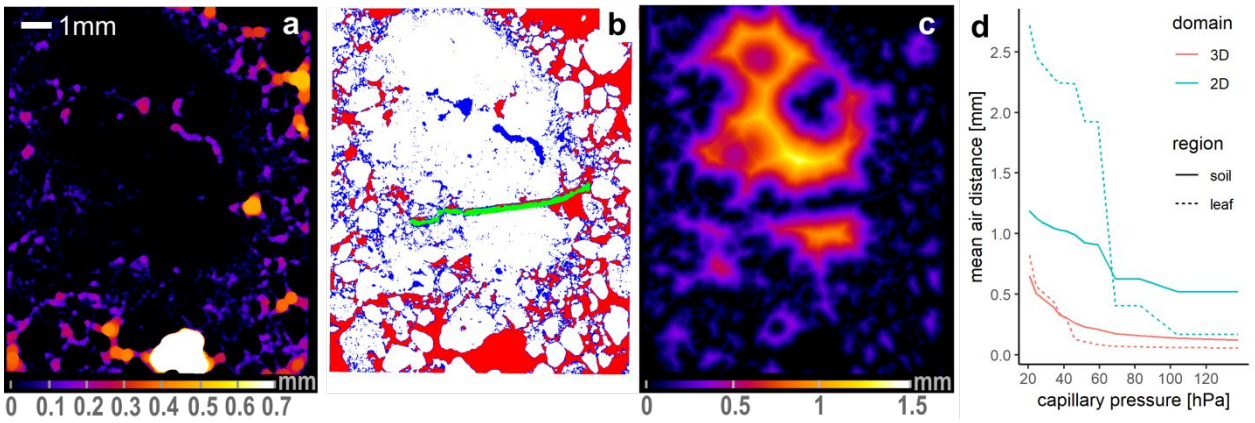

Figure 2: (a) 3D pore size distribution depicted in the 2D reference plane. (b) Modeled distribution of water (blue) and air (red) at a capillary pressure of 50 hPa. Soil and leaf are shown in white and green. (c) 3D Euclidean distance towards air-filled pores at a capillary pressure of 50 hPa. (d) Mean air distance as a function of capillary pressure for the entire soil or the leaf only. Air distribution is either modelled in 3D and 3D distances registered into the LM plane or modelled in 2D on the registered, segmented image.

Such modelled air distances in the LM plane would be vastly overestimated if 3D structural information is not available. The main reasons are that (1) air continuity through the third dimension is lost and that (2) air-filled pores in close vicinity are ignored, when they are outside of the plane. Even if the connectivity rule is relaxed from the top boundary to all four boundaries, the mean 2D air distances in soil still range from 1.19 mm to 0.52 mm in the investigated capillary pressure range, a three to four fold increase (Figure 2d). Also the critical value to overcome the air-entry pressure of the gap in the vicinity of the leaf is only reached at 70hPa. The reduction in dimensionality always leads to an overestimation of diffusion distances through the water-filled soil matrix. However, the magnitude depends on water saturation and bulk density. Expanding the modelled capillary range to higher capillary pressure could only be achieved with higher image resolution (<7µm) which comes at the expense of smaller sample size. However, it can also be extended by evaluating the pore space in SEM images[28] (see below).

Measuring the actual air-water distribution with X-ray CT should always be favored over 3D modelling, since it has become a routine operation even without contrast agents[29, 30]. If possible, CT scans could be carried out twice, once at the water content of interest and once more after resin impregnation to recover any internal deformation that may occur during fluid displacement and resin curing. Methods for deformation analysis are elastic registration or digital volume correlation[31, 32]. Finally, there are also resin impregnation protocols that maintain the location of fluid interfaces by sequential application of two differently dyed resins[33]. However this approach has not been adopted in soil science yet.

3.2. Microhabitats

All 2D biogeochemical microscopy results only need to be registered to the LM plane to project co-registered 3D structural information onto them. This is shown for the double excitation fluorescence microscopy results in the supporting information (S2), which map the auto-fluorescence intensity as a result of local concentrations in plant tissue and other organic compounds. Furthermore, this is shown for blue-excitation fluorescence microscopy (FM) including the cell count results (Figure 3a). Cells counted in 2D thin sections (n=536) corresponded to cell numbers of 1×10^7 cells g^{-1} soil. This is estimated from the area of the FM scene (19.91 mm²), the representative observation depth (1 µm) and bulk density (1.3 g/cm³). Individual bacteria are visible in the enlarged region (Figure 3b), that was subsequently chosen for chemical microscopy. The spatial analysis reveals that bacteria tend to be located near the leaf, which is indicated by a distance ratio of 0.75. That is, a randomly chosen cell has only 75% of the 3D Euclidean distance to the nearest leaf surface as compared to the average leaf distance in the FM image. For this metric the bias caused by only considering 2D leaf distances vanished completely, since the LM plane is oriented roughly normal to the leaf and there is no additional leaf fragment located out of plane. Bacteria also have a preference to reside near pore surfaces with a distance ratio of 0.78. This supports previous findings[34] showing that pore surface preference was strongly developed in subsoil samples of a sandy silt loam, but less evident in the topsoil. One reason for this preference is that bacteria are directly attached to surfaces of air-filled

macropores[35, 36], be it in biofilms or open, water-filled capillaries along rough surfaces. Furthermore, cells in bigger pores are moved towards the pore surface when fluids are replaced during sample preparation[14]. Another explanation is that bacteria in the water-filled soil matrix are more abundant at oxic sites near air-filled pores than at anoxic sites with longer diffusion distances of dissolved oxygen[37]. Note that the site preference to visible macropores is also evident if only cells within invisible mesopores are considered (data not shown) which rules out a simple sample preparation artifact. The difference between 3D and 2D distances ratios is again negligible for pore surfaces, this time because the plane is densely populated with many pore surfaces of presumably isotropic shape, so the 2D plane is representative for its proximal 3D vicinity. The absolute distances are larger in 2D than in 3D, but the ratios are comparable.

The spatial distribution of bacteria can also be characterized with respect to the size of pores in which they are located. Roughly 75% of all detected bacteria were found in unresolved mesopores, which are known for their favorable micro-environmental conditions for bacteria [38-40]. Switching from co-registered 3D pore sizes in the LM plane to maximum inscribed circles computed in the 2D plane has hardly any effect on unresolved mesopores, but increases the area fraction of macropores on the expense of narrow macropores. This is a general trend, because obstacles within bigger pores, which are outside of the plane, are ignored with the maximum inscribed circle method in 2D.

In summary, the combination of 3D structural information with 2D fluorescence microscopy opens up completely new avenues for the characterization of soil microbial habitats. The spatial distribution of bacteria are not only analyzed with respect to each other[41], but with respect to their environment[14, 34]. Note that segmentation into pores and background could have also been done on the FM image directly[34], as the difference between distance ratios in 3D and 2D were tolerable. However, pore segmentation is much easier with X-ray CT as it directly reflects the local electron density without out-of-focus and illumination artifacts. Comparable results between 3D and 2D pore space attributes like porosity and pore surface area in microbial habitats were also reported in ref.[14]. We have demonstrated that large differences between 2D and 3D may arise in pore space attributes that rely on pore continuity like drainage processes. In that case a correlative imaging approach with X-ray microtomography is superior to microhabitat characterization with FM only. We showed that bacteria were more abundant in the detritusphere hot spot of a decaying plant leaf, most abundant in mesopores and had a higher site preference for pore surfaces.

The selected DAPI stain, which binds to all accessible DNA, was applied directly on the polished surface after resin impregnation in order to be readily integrated in our imaging pipeline. Combinations with dyes that selectively bind to active or dead cells are feasible[42, 43], but those need to be applied during incubation to interact with the cells. Moreover, phyla-specific cell detection via fluorescence in situ hybridization (FISH) with different probes may reveal differences in microhabitats (e.g. bacteria vs. archaea)[44], which can also be combined with information of microbial activity using isotopic tracing[45-48]. Finally, microbiological techniques

329 and isotope enrichment can be used to track metabolic activity of individual cells in their
330 microenvironments via mapping with secondary ion mass spectrometry as described below.

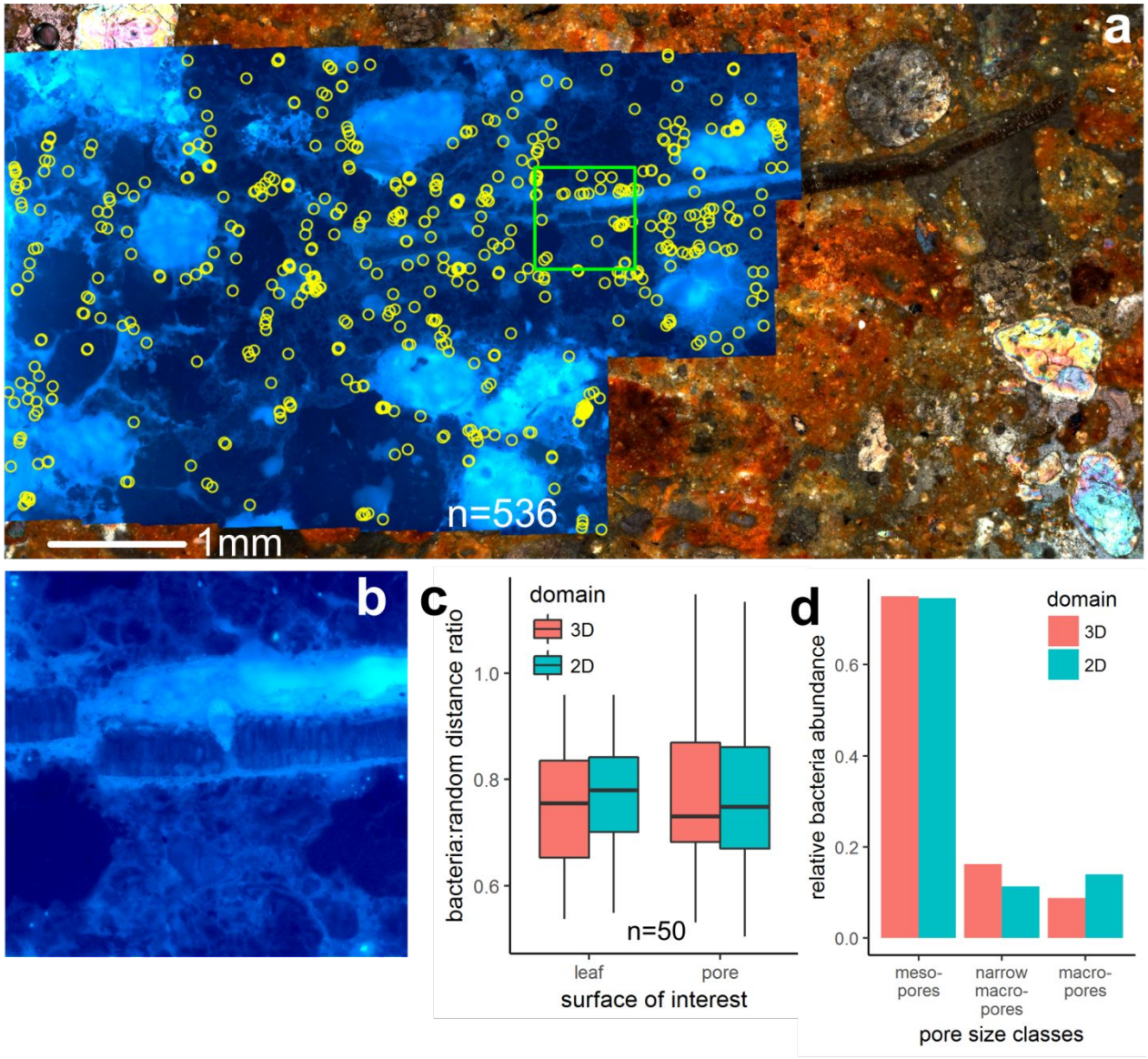

331

332 **Figure 3: (a) 2D-2D image registration with fluorescence microscopy (FM) and light microscopy (LM). Yellow circles**
333 **indicate the spatial distribution of bacteria. The green frame indicates the region enlarged in (b) that was chosen for**
334 **chemical microscopy in Figure 4. (c) Bacteria distances to the leaf surface or pore surfaces are normalized by distances of**
335 **randomly chosen points to these surfaces. The data represents 30 samples comprising 30 locations each.**

336 ## 3.3. Chemical microscopy

337 The backscattered electron microscopy image provides a very good material contrast between
338 mineral particles and the resin to differentiate between pores and soil material. Also the leaf is
339 clearly visible due to distinct small-scale structures of the tissue (plant cells) within an otherwise
340 homogeneous resin (Figure 4a). The dark stripes in the center were caused by prior NanoSIMS
341 imaging due to the sputtering process which removes the Au/Pd layer and thus slightly changes

the material contrast of the sample surface, which is a useful effect to relocate NanoSIMS measurements using SEM. Both transects were analyzed using NanoSIMS (Figure 4d), whereas the left transect was a test measurement. SEM provides a good alternative as a bridging technique for image registration, the more so since direct attempts to register NanoSIMS images into the LM plane failed (data not shown) due to the scale gap between the LM images and the small field of view of the NanoSIMS measurements. It was only successful by means of an additional light microscopy image with only one depth of focus directly targeted at the surface roughness of the resin so that crevices in the resin could be used for corresponding landmarks (Figure 4d). This auxiliary LM image can then be used to align the NanoSIMS transect to the LM image of the entire plane in a second image registration step.

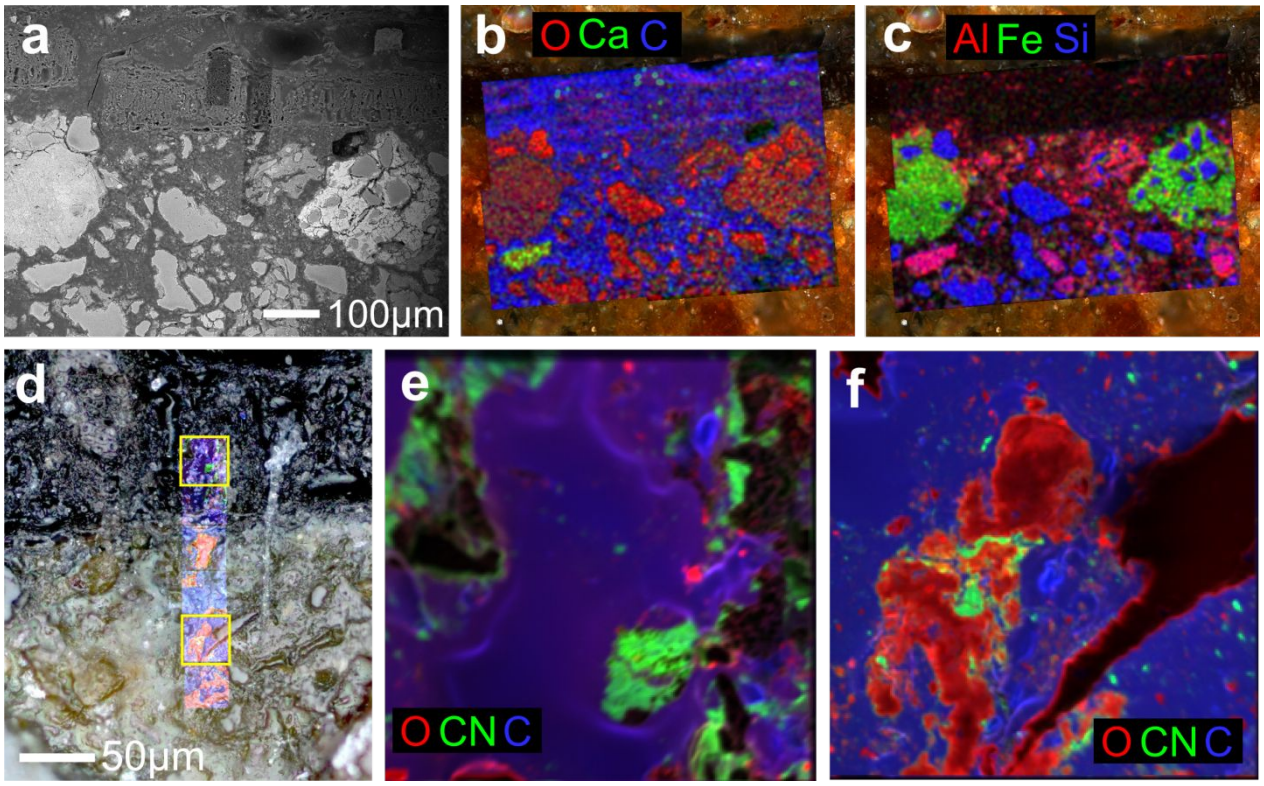

Figure 4: (a) unregistered SEM image in back-scattered mode. (b-c) Registered SEM-EDX image showing six elemental distributions in different colors. (d) NanoSIMS transect registered to an auxiliary LM image with depth focus on resin surface. (e-f) Overlay of three ion channels for two scenes in the transect highlighted with a yellow frame in (d).

The SEM-EDX elemental maps are easily registered into the LM plane by using the O- or C-channel with good contrast between mineral particles and the resin (Figure 4b). The resulting transformation matrix can then be employed on other elemental maps that do not contain sufficient structural information like the Ca-channel (Figure 4b). The elemental inventory obtained through SEM-EDX shows a heterogeneous distribution of element concentrations at a small scale (Figure 4b-c). Two iron-rich micro-aggregates contain several smaller, sharply delineated Si-rich minerals, presumably quartz grains encrusted in iron oxide concretions, a feature reported before for Quartz grains within macro-aggregates [49]. The soil matrix is composed of a mix between Si-rich (quartz) and Al-rich particles (feldspars, clay minerals). High

concentrations of Ca are highly localized, either in the leaf or in individual particles. First attempts have been made to use the correlation between µCT attenuation values and co-located element intensities to extrapolate elemental maps into 3D space via co-kriging[50]. This is an elegant approach to fully exploit the potential of correlative imaging.

It was conjectured that the O:C ratio obtained from SEM-EDX could be used to distinguish particulate organic matter from the resin[50]. However, our attempts failed (data not shown). NanoSIMS imaging is a viable alternative in this regard due to the high sensitivity for the detection of organic matter specific $^{12}C^{14}N$ and ^{12}C secondary ion species. In contrast to SEM-EDX, this technique can visualize nitrogen distributions and thus map organic matter (OM) through the detection of cyanide secondary ions ($^{12}C^{14}N$)[51], which is at very low concentrations in the used epoxy resin. In this transect OM mainly occurs as leaf tissue (Figure 4e) or is occluded in microaggregates (Figure 4f). The high $^{12}C^{14}N$ ion counts at the leaf or particulate organic matter surface and within the microaggregate clearly point to a distinct amount of microbial derived OM[52] . Thus the leaf detritusphere providing easily available substrates supports microbial activity and fosters microaggregate formation by microbial residues as gluing agents[18, 53]. This finding correlates well with the higher bacterial cell numbers in the vicinity of the particulate organic matter (Figure 3). Such NanoSIMS transects along a gradient of microenviromental conditions are a formidable tool to detect rhizodeposits through ^{13}C labeling [53, 54], map zones of different redox conditions across the rhizosphere in paddy soils[55] or identify different functional domains with soil aggregates with respect to carbon sequestration and nutrient cycling[49].

4. Acknowledgments

This study was funded by the Deutsche Forschungsgemeinschaft through the research unit DFG-FOR 2337: Denitrification in Agricultural Soils: Integrated Control and Modelling at Various Scales (DASIM). We thank Gertraut Harrington for sample preparation, Max Koehne for CT scanning and Philippe Baveye for inspiring discussions during the preparation of the paper. We are grateful to three anonymous reviewers for the valuable comments.

5. Supporting information:

S1 - Detailed Description of Drainage Model,

S2 - Mapping organic compounds with double-excitation fluorescence microscopy

S3 – File link and description of minimum example for 2D-3D registration with Elastix

6. References

1. Lehmann, J.; Kleber, M., The contentious nature of soil organic matter. *Nature* **2015,** *528*, 60.

2. Dungait, J. A. J.; Hopkins, D. W.; Gregory, A. S.; Whitmore, A. P., Soil organic matter turnover is governed by accessibility not recalcitrance. *Global Change Biology* **2012,** *18*, (6), 1781-1796.
3. Schimel, J.; Schaeffer, S., Microbial control over carbon cycling in soil. *Frontiers in Microbiology* **2012,** *3*, (348), 1-11.
4. Vos, M.; Wolf, A. B.; Jennings, S. J.; Kowalchuk, G. A., Micro-scale determinants of bacterial diversity in soil. *FEMS Microbiology Reviews* **2013,** *37*, (6), 936-954.
5. Tecon, R.; Or, D., Biophysical processes supporting the diversity of microbial life in soil. *FEMS Microbiology Reviews* **2017,** *41*, (5), 599-623.
6. Kuzyakov, Y.; Blagodatskaya, E., Microbial hotspots and hot moments in soil: Concept & review. *Soil Biology and Biochemistry* **2015,** *83*, 184-199.
7. Baveye, P. C.; Otten, W.; Kravchenko, A.; Balseiro-Romero, M.; Beckers, É.; Chalhoub, M.; Darnault, C.; Eickhorst, T.; Garnier, P.; Hapca, S.; Kiranyaz, S.; Monga, O.; Mueller, C. W.; Nunan, N.; Pot, V.; Schlüter, S.; Schmidt, H.; Vogel, H.-J., Emergent Properties of Microbial Activity in Heterogeneous Soil Microenvironments: Different Research Approaches Are Slowly Converging, Yet Major Challenges Remain. *Frontiers in Microbiology* **2018,** *9*, (1929), 1-48.
8. Young, I. M.; Crawford, J. W., Interactions and Self-Organization in the Soil-Microbe Complex. *Science* **2004,** *304*, 1634-1637.
9. Cnudde, V.; Boone, M. N., High-resolution X-ray computed tomography in geosciences: A review of the current technology and applications. *Earth-Science Reviews* **2013,** *123*, (0), 1-17.
10. Wildenschild, D.; Sheppard, A. P., X-ray imaging and analysis techniques for quantifying pore-scale structure and processes in subsurface porous medium systems. *Advances in Water Resources* **2013,** *51*, (0), 217-246.
11. Helliwell, J. R.; Sturrock, C. J.; Grayling, K. M.; Tracy, S. R.; Flavel, R. J.; Young, I. M.; Whalley, W. R.; Mooney, S. J., Applications of X-ray computed tomography for examining biophysical interactions and structural development in soil systems: a review. *European Journal of Soil Science* **2013,** *64*, (3), 279-297.
12. Handschuh, S.; Baeumler, N.; Schwaha, T.; Ruthensteiner, B., A correlative approach for combining microCT, light and transmission electron microscopy in a single 3D scenario. *Frontiers in Zoology* **2013,** *10*, (1), 44.
13. Caplan, J.; Niethammer, M.; Taylor, R. M.; Czymmek, K. J., The power of correlative microscopy: multi-modal, multi-scale, multi-dimensional. *Current Opinion in Structural Biology* **2011,** *21*, (5), 686-693.
14. Juyal, A.; Otten, W.; Falconer, R.; Hapca, S.; Schmidt, H.; Baveye, P. C.; Eickhorst, T., Combination of techniques to quantify the distribution of bacteria in their soil microhabitats at different spatial scales. *Geoderma* **2019,** *334*, 165-174.
15. Hapca, S. M.; Wang, Z. X.; Otten, W.; Wilson, C.; Baveye, P. C., Automated statistical method to align 2D chemical maps with 3D X-ray computed micro-tomographic images of soils. *Geoderma* **2011,** *164*, (3-4), 146-154.
16. Klein, S.; Staring, M.; Murphy, K.; Viergever, M. A.; Pluim, J. P. W., elastix: A Toolbox for Intensity-Based Medical Image Registration. *Medical Imaging, IEEE Transactions on* **2010,** *29*, (1), 196-205.
17. Shamonin, D.; Bron, E.; Lelieveldt, B.; Smits, M.; Klein, S.; Staring, M., Fast Parallel Image Registration on CPU and GPU for Diagnostic Classification of Alzheimer's Disease. *Frontiers in Neuroinformatics* **2014,** *7*, (50), 1-15.
18. Mueller, C. W.; Hoeschen, C.; Steffens, M.; Buddenbaum, H.; Hinkel, K.; Bockheim, J. G.; Kao-Kniffin, J., Microscale soil structures foster organic matter stabilization in permafrost soils. *Geoderma* **2017,** *293*, 44-53.

19. Mueller, C. W.; Weber, P. K.; Kilburn, M. R.; Hoeschen, C.; Kleber, M.; Pett-Ridge, J., Chapter One - Advances in the Analysis of Biogeochemical Interfaces: NanoSIMS to Investigate Soil Microenvironments. In *Advances in Agronomy*, Sparks, D. L., Ed. Academic Press: 2013; Vol. 121, pp 1-46.
20. Schlüter, S.; Sheppard, A.; Brown, K.; Wildenschild, D., Image processing of multiphase images obtained via X-ray microtomography: A review. *Water Resources Research* **2014,** *50*, (4), 3615-3639.
21. Schindelin, J.; Arganda-Carreras, I.; Frise, E.; Kaynig, V.; Longair, M.; Pietzsch, T.; Preibisch, S.; Rueden, C.; Saalfeld, S.; Schmid, B., Fiji: an open-source platform for biological-image analysis. *Nature methods* **2012,** *9*, (7), 676-682.
22. Vogel, H.-J.; Weller, U.; Schlüter, S., Quantification of soil structure based on Minkowski functions. *Computers & Geosciences* **2010,** *36*, (10), 1236-1245.
23. Polerecky, L.; Adam, B.; Milucka, J.; Musat, N.; Vagner, T.; Kuypers, M. M. M., Look@NanoSIMS – a tool for the analysis of nanoSIMS data in environmental microbiology. *Environmental Microbiology* **2012,** *14*, (4), 1009-1023.
24. Hazlett, R. D., Simulation of capillary-dominated displacements in microtomographic images of reservoir rocks. *Transport in Porous Media* **1995,** *20*, (1-2), 21-35.
25. Legland, D.; Arganda-Carreras, I.; Andrey, P., MorphoLibJ: integrated library and plugins for mathematical morphology with ImageJ. *Bioinformatics* **2016,** *32*, (22), 3532-3534.
26. Schmidt, H.; Nunan, N.; Höck, A.; Eickhorst, T.; Kaiser, C.; Woebken, D.; Raynaud, X., Recognizing Patterns: Spatial Analysis of Observed Microbial Colonization on Root Surfaces. *Frontiers in Environmental Science* **2018,** *6*, (61), 1-12.
27. Mattes, D.; Haynor, D. R.; Vesselle, H.; Lewellyn, T. K.; Eubank, W., Nonrigid multimodality image registration. In *Proc. SPIE*, San Diego, CA, 2001; Vol. 4322, pp 1609-1620.
28. Latham, S.; Varslot, T.; Sheppard, A., Image Registration: Enhancing and Calibrating X-ray Micro-CT Imaging. In *Proceedings of the Society of Core Analysis, Abu Dhabi, UAE, October 2008*, Abu Dhabi, UAE, 2008.
29. Kumahor, S.; de Rooij, G.; Schlüter, S.; Vogel, H.-J., Water Flow and Solute Transport in Unsaturated Sand--A Comprehensive Experimental Approach. *Vadose Zone Journal* **2015,** *14*.
30. Geistlinger, H.; Mohammadian, S.; Schlueter, S.; Vogel, H.-J., Quantification of capillary trapping of gas clusters using X-ray microtomography. *Water Resources Research* **2014,** *50*, (5), 4514-4529.
31. Schlüter, S.; Leuther, F.; Vogler, S.; Vogel, H.-J., X-ray microtomography analysis of soil structure deformation caused by centrifugation. *Solid Earth* **2016,** *7*, (1), 129-140.
32. Peth, S.; Nellesen, J.; Fischer, G.; Horn, R., Non-invasive 3D analysis of local soil deformation under mechanical and hydraulic stresses by μCT and digital image correlation. *Soil and Tillage Research* **2010,** *111*, (1), 3-18.
33. Seth, S.; Morrow, N. R.; others, Efficiency of the conversion of work of drainage to surface energy for sandstone and carbonate. *SPE Reservoir Evaluation & Engineering* **2007,** *10*, (04), 338-347.
34. Nunan, N.; Wu, K.; Young, I. M.; Crawford, J. W.; Ritz, K., Spatial distribution of bacterial communities and their relationships with the micro-architecture of soil. *FEMS Microbiology Ecology* **2003,** *44*, (2), 203-215.
35. Or, D.; Smets, B. F.; Wraith, J. M.; Dechesne, A.; Friedman, S. P., Physical constraints affecting bacterial habitats and activity in unsaturated porous media - a review. *Advances in Water Resources* **2007,** *30*, (6-7), 1505-1527.
36. Flemming, H.-C.; Wingender, J.; Szewzyk, U.; Steinberg, P.; Rice, S. A.; Kjelleberg, S., Biofilms: an emergent form of bacterial life. *Nature Reviews Microbiology* **2016,** *14*, 563.

37. Horn, R.; Stepniewski, W.; Wlodarczyk, T.; Walenzik, G.; Eckhardt, F., Denitrification rate and microbial distribution within homogeneous model soil aggregates. *Int. Agrophysics* **1994,** *8*, 65-74.
38. Crawford, J. W.; Deacon, L.; Grinev, D.; Harris, J. A.; Ritz, K.; Singh, B. K.; Young, I., Microbial diversity affects self-organization of the soil-microbe system with consequences for function. *Journal of The Royal Society Interface* **2012,** *9*, (71), 1302-1310.
39. Negassa, W. C.; Guber, A. K.; Kravchenko, A. N.; Marsh, T. L.; Britton, H.; Rivers, M. L., Properties of Soil Pore Space Regulate Pathways of Plant Residue Decomposition and Community Structure of Associated Bacteria. *PLoS ONE* **2015,** *10*, (4), 1-22.
40. Akbari, A.; Ghoshal, S., Bioaccessible Porosity in Soil Aggregates and Implications for Biodegradation of High Molecular Weight Petroleum Compounds. *Environmental Science & Technology* **2015,** *49*, (24), 14368-14375.
41. Raynaud, X.; Nunan, N., Spatial Ecology of Bacteria at the Microscale in Soil. *PLOS ONE* **2014,** *9*, (1), e87217.
42. Blagodatskaya, E.; Kuzyakov, Y., Active microorganisms in soil: Critical review of estimation criteria and approaches. *Soil Biology and Biochemistry* **2013,** *67*, 192-211.
43. Emerson, J. B.; Adams, R. I.; Román, C. M. B.; Brooks, B.; Coil, D. A.; Dahlhausen, K.; Ganz, H. H.; Hartmann, E. M.; Hsu, T.; Justice, N. B.; Paulino-Lima, I. G.; Luongo, J. C.; Lymperopoulou, D. S.; Gomez-Silvan, C.; Rothschild-Mancinelli, B.; Balk, M.; Huttenhower, C.; Nocker, A.; Vaishampayan, P.; Rothschild, L. J., Schrödinger's microbes: Tools for distinguishing the living from the dead in microbial ecosystems. *Microbiome* **2017,** *5*, (1), 86.
44. Eickhorst, T.; Tippkötter, R., Improved detection of soil microorganisms using fluorescence in situ hybridization (FISH) and catalyzed reporter deposition (CARD-FISH). *Soil Biology and Biochemistry* **2008,** *40*, (7), 1883-1891.
45. Musat, N.; Foster, R.; Vagner, T.; Adam, B.; Kuypers, M. M. M., Detecting metabolic activities in single cells, with emphasis on nanoSIMS. *FEMS Microbiology Reviews* **2012,** *36*, (2), 486-511.
46. Pett-Ridge, J.; Weber, P. K., NanoSIP: NanoSIMS applications for microbial biology. *Methods in molecular biology (Clifton, N.J.)* **2012,** *881*, 375-408.
47. Eichorst, S. A.; Strasser, F.; Woyke, T.; Schintlmeister, A.; Wagner, M.; Woebken, D., Advancements in the application of NanoSIMS and Raman microspectroscopy to investigate the activity of microbial cells in soils. *FEMS Microbiology Ecology* **2015,** *91*, (10), fiv106.
48. Tominski, C.; Lösekann-Behrens, T.; Ruecker, A.; Hagemann, N.; Kleindienst, S.; Mueller, C. W.; Höschen, C.; Kögel-Knabner, I.; Kappler, A.; Behrens, S., Insights into Carbon Metabolism Provided by Fluorescence In Situ Hybridization-Secondary Ion Mass Spectrometry Imaging of an Autotrophic, Nitrate-Reducing, Fe(II)-Oxidizing Enrichment Culture. *Applied and Environmental Microbiology* **2018,** *84*, (9).
49. Steffens, M.; Rogge, D. M.; Mueller, C. W.; Höschen, C.; Lugmeier, J.; Kölbl, A.; Kögel-Knabner, I., Identification of Distinct Functional Microstructural Domains Controlling C Storage in Soil. *Environmental Science & Technology* **2017,** *51*, (21), 12182-12189.
50. Hapca, S.; Baveye, P. C.; Wilson, C.; Lark, R. M.; Otten, W., Three-Dimensional Mapping of Soil Chemical Characteristics at Micrometric Scale by Combining 2D SEM-EDX Data and 3D X-Ray CT Images. *PLoS ONE* **2015,** *10*, (9), e0137205.
51. Schweizer, S., A.; Hoeschen, C.; Schlüter, S.; Kögel-Knabner, I.; Mueller, C., W., Rapid soil formation after glacial retreat shaped by spatial patterns of organic matter accrual in microaggregates. *Global Change Biology* **2018,** *24*, (4), 1637-1650.

541 52. Hatton, P.-J.; Remusat, L.; Zeller, B.; Derrien, D., A multi-scale approach to determine
542 accurate elemental and isotopic ratios by nano-scale secondary ion mass spectrometry imaging.
543 *Rapid Communications in Mass Spectrometry* **2012,** *26*, (11), 1363-1371.
544 53. Vidal, A.; Hirte, J.; Bender, S. F.; Mayer, J.; Gattinger, A.; Höschen, C.; Schädler, S.;
545 Iqbal, T. M.; Mueller, C. W., Linking 3D Soil Structure and Plant-Microbe-Soil Carbon Transfer
546 in the Rhizosphere. *Frontiers in Environmental Science* **2018,** *6*, (9), 1-14.
547 54. Clode, P. L.; Kilburn, M. R.; Jones, D. L.; Stockdale, E. A.; Cliff, J. B.; Herrmann, A. M.;
548 Murphy, D. V., In situ mapping of nutrient uptake in the rhizosphere using nanoscale sceondary
549 ion mass spectrometry. *Plant Physiology* **2009,** *151*, 1751-1757.
550 55. Kölbl, A.; Schweizer, S.; Mueller, C.; Höschen, C.; Said-Pullicino, D.; Romani, M.;
551 Lugmeier, J.; Schlüter, S.; Kögel-Knabner, I., Legacy of Rice Roots as Encoded in Distinctive
552 Microsites of Oxides, Silicates, and Organic Matter. *Soils* **2017,** *1*, (1), 2.

553

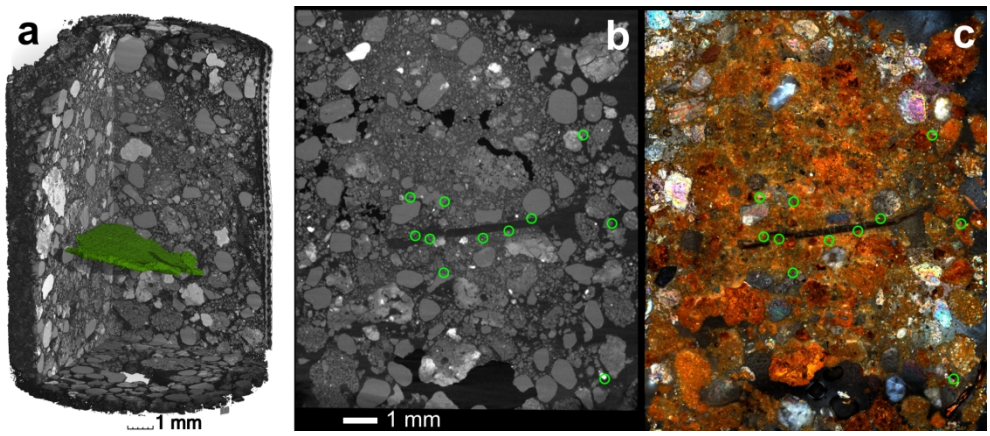

Figure 1: (a) X-ray CT scan with the embedded leaf in green. (b) 2D-3D registration and (c) the reference microscopy image that was used as a target for image registration. Eleven landmarks (green circles) were used for image registration.

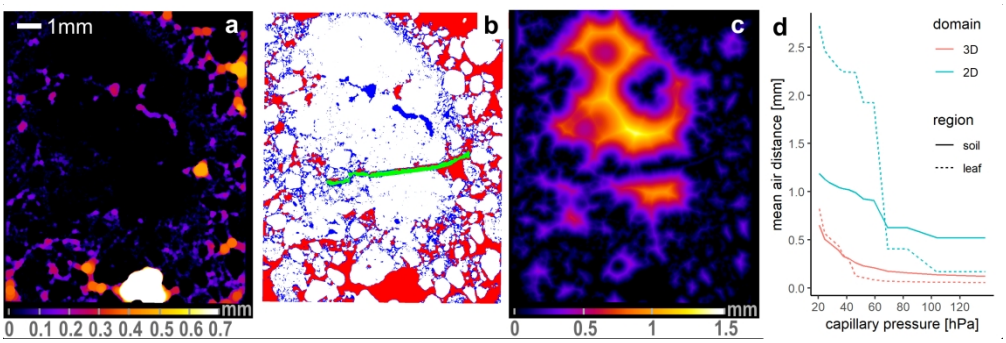

Figure 2: (a) 3D pore size distribution depicted in the 2D reference plane. (b) Modeled distribution of water (blue) and air (red) at a capillary pressure of 50 hPa. Soil and leaf are shown in white and green. (c) 3D Euclidean distance towards air-filled pores at a capillary pressure of 50 hPa. (d) Mean air distance as a function of capillary pressure for the entire soil or the leaf only. Air distribution is either modelled in 3D and 3D distances registered into the LM plane or modelled in 2D on the registered, segmented image.

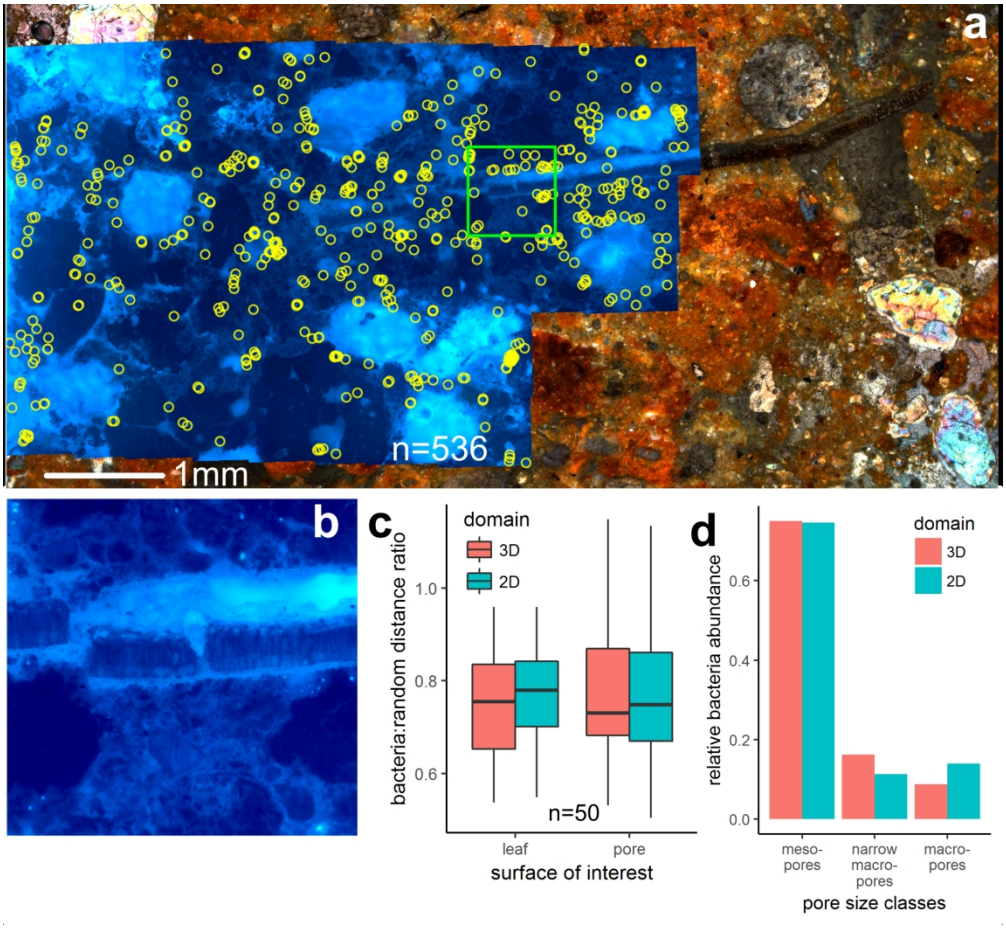

Figure 3: (a) 2D-2D image registration with fluorescence microscopy (FM) and light microscopy (LM). Yellow circles indicate the spatial distribution of bacteria. The green frame indicates the region enlarged in (b) that was chosen for chemical microscopy in Figure 4. (c) Bacteria distances to the leaf surface or pore surfaces are normalized by distances of randomly chosen points to these surfaces. The data represents 30 samples comprising 30 locations each.

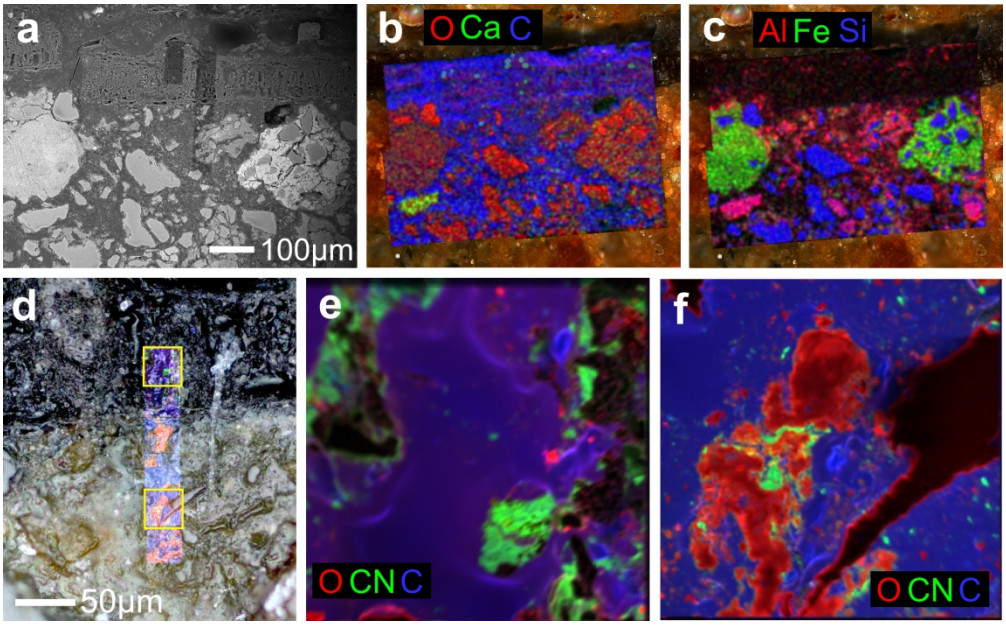

Figure 4: (a) unregistered SEM image in back-scattered mode. (b-c) Registered SEM-EDX image showing six elemental distributions in different colors. (d) NanoSIMS transect registered to an auxiliary LM image with depth focus on resin surface. (e-f) Overlay of three ion channels for two scenes in the transect highlighted with a yellow frame in (d).

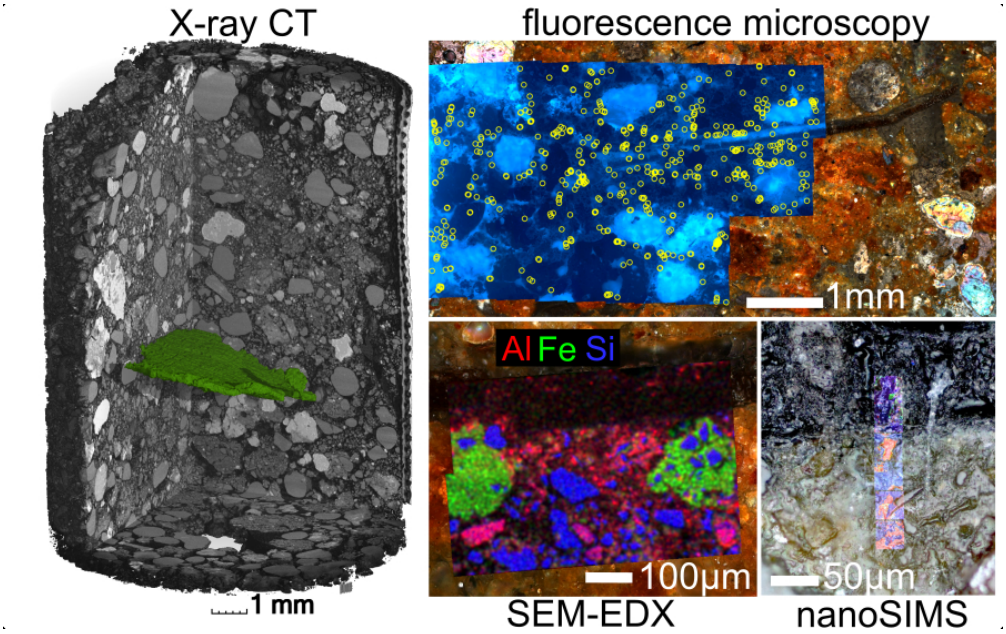
X-ray CT
fluorescence microscopy
1 mm
1mm
Al Fe Si
100µm
50µm
SEM-EDX
nanoSIMS

TOC art